Millisecond-order X-ray phase tomography with a fringe-scanning method

doi: 10.7567/APEX.11.122501

Applied Physics Express **11**, 122501 (2018)
https://doi.org/**10.7567/APEX.11.122501**

Millisecond-order X-ray phase tomography with a fringe-scanning method

Wataru Yashiro[1], Chika Kamezawa[1,2], Daiji Noda[3], and Kentaro Kajiwara[4]

[1]*Institute of Multidisciplinary Research for Advanced Materials (IMRAM), Tohoku University, Sendai 980-8577, Japan*
[2]*Department of Materials Structure Science, SOKENDAI (The Graduate University for Advanced Studies), Tsukuba, Ibaraki 305-0801, Japan*
[3]*Micromachine Center (MMC), Chiyoda, Tokyo 101-0026, Japan*
[4]*Japan Synchrotron Radiation Research Institute (JASRI), Sayo, Hyogo 679-5198, Japan*

Received August 22, 2018; accepted October 14, 2018; published online October 31, 2018

We successfully realized millisecond-order X-ray phase tomography using a fringe-scanning method in grating-based X-ray interferometry. We obtained phase tomograms with a measurement time of 4.43 ms using a white synchrotron X-ray beam. The use of a fringe-scanning method enables us to achieve not only a higher spatial resolution but also a higher signal-to-noise ratio than that attained by the Fourier transform method. In addition, our approach can be applied to realize four-dimensional or high-throughput X-ray tomography for samples that can be rotated at a high speed. © 2018 The Japan Society of Applied Physics

The demand for imaging techniques that facilitate the examination of the internal structures of a sample with high temporal and spatial resolution has steadily increased in fields ranging from material science to the life sciences, with the need to characterize increasingly intricate structures. High-speed X-ray tomography can potentially address this demand. However, an improvement in sensitivity and the use of a high-flux X-ray beam are required to achieve high temporal resolution without sacrificing the spatial resolution because there is generally a tradeoff between temporal and spatial resolution in imaging.

X-ray phase-contrast imaging techniques based on X-ray phase shift caused by refraction can facilitate an improvement in sensitivity: they have much higher sensitivities than conventional X-ray absorption.[1–3] Two X-ray phase-contrast imaging techniques have thus far been applied to high-speed X-ray imaging. One is the propagation-based imaging (PBI), which uses enhanced edge contrast during the free-space propagation of X-rays.[4–6] A temporal resolution on the order of or less than 10 μs is possible because this technique enables the use of a white or pink synchrotron X-ray beam.[7–13] However, for quantitative imaging, which is required for tomographic reconstruction, a quasi-homogeneous assumption is necessary. The other technique for high-speed X-ray imaging is grating-based X-ray imaging, which has been spotlighted since the early 2000s.[14–36] This technique uses gratings to realize X-ray phase-contrast imaging and can be utilized with a white synchrotron X-ray beam, which permits a temporal resolution comparable to that of the PBI technique.[12,33,34] In addition, its multimodality can facilitate the acquisition of not only quantitative images for X-ray phase shift (a quantitative differential-phase image) which is an essential requirement for quantitative phase tomography, but also two other images: a transmittance image, which is an edge-enhanced image that is equivalent to that obtained by PBI,[31] and a normalized visibility image with contrast that is primarily attributable to ultra-small-angle X-ray scattering.[20,24,31,32,35] For these reasons, the grating-based X-ray-imaging technique is promising for high-speed tomography.

In previous papers, we reported on the successful realization of X-ray phase tomography with an acquisition time of less than 10 ms using grating-based X-ray imaging with a white synchrotron X-ray beam.[33,34] We used the so-called Fourier transform method[37] to obtain the three images from a moiré image obtained using grating-based X-ray interferometry. However, because the spatial resolution of the acquired three images is determined by the pitch of the fringes in the moiré image, a high-spatial resolution requires a fine pitch of moiré fringes, which generally causes a reduction in the visibility of the fringes because of the finite spatial resolution of the X-ray detector. It should be noted that a higher spatial resolution causes a lower signal-to-noise ratio of a differential-phase image based on the Fourier transform method because the signal-to-noise ratio of a differential-phase image is linearly proportional to the visibility.[19,36]

In this paper, we report on millisecond-order X-ray phase tomography using a fringe scanning method.[38–40] In a fringe scanning method, three or more moiré images are required to obtain the three images. As such, three or more turns of a sample with a continuously moving grating is necessary to realize high-speed X-ray phase tomography. In other words, both a higher rotation speed of the sample and a higher frame rate of the X-ray image detector are required in a fringe scanning method to achieve a temporal resolution comparable to the Fourier transform method. However, a fringe scanning method has the advantage of a higher spatial resolution, which is mainly determined by the spatial resolution of the X-ray image detector, and a higher visibility for moiré fringes with a large pitch, resulting in a higher signal-to-noise ratio for differential-phase images. In a published report, Kibayashi et al. reported that they realized X-ray phase tomography using a fringe scanning method with a measurement time of 5 s.[29] In this paper, we report on the successful realization X-ray phase tomography using a fringe scanning method with a measurement time of 4.43 ms. The proposed approach can be applied to achieve four-dimensional or high-throughput X-ray tomography for samples that can be rotated at a high speed.

Figure 1 shows the experimental setup for millisecond-order X-ray tomography using a fringe scanning method, which is basically the same as that reported in a previous paper,[34] except that the second grating (G2) is continuously moved. An X-ray grating interferometer consisting of two gratings (G1 and G2) was constructed in an experimental station of BL28B2, SPring-8, where a white synchrotron X-ray beam from a bending magnet source is available. The source size [full width at half maximum (FWHM)] of the white synchrotron X-ray beam in the vertical direction was designed to be 28.7 μm.[41] A gold $\pi/2$-phase grating designed for an X-ray energy of 25 keV and a gold absorption grating with a thickness of 60 μm were used as the first (G1) and

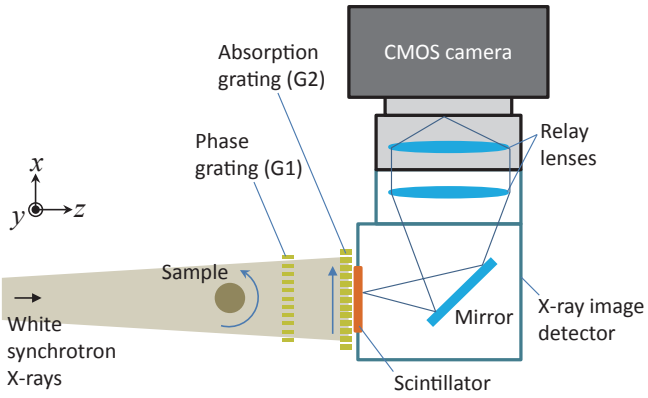

Fig. 1. Experimental setup of X-ray grating interferometer for millisecond-order X-ray phase tomography using fringe scanning method.

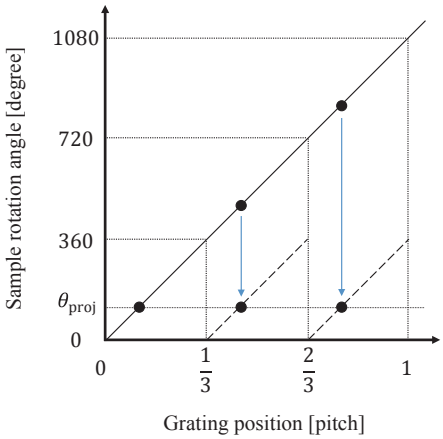

Fig. 2. Image acquisition sequence (relationship between sample rotation angle and grating position).

second (G2) gratings, respectively. The pitch of the two gratings was 5.3 μm. G1 was located 44 m downstream of the source, and the distance between G1 and G2 was set to 283 mm, corresponding to a Talbot order of 0.5 for 25 keV. Both gratings were fabricated on 200-μm-thick Si substrates. The lines of G1 were aligned in the horizontal direction (y-direction) because of the smaller source size in the vertical direction, and G2 was aligned parallel to the lines of G1 to generate parallel moiré fringes with a large pitch. A sample which was located 135 mm upstream of G1 was rotated using a DC motor with a high speed around the horizontal direction while G2 was continuously moved in the vertical direction.

An X-ray image detector consisting of a scintillator screen, lenses, and a high-speed CMOS camera (Photoron FASTCAM MiniAX100), was located behind G2 to capture moiré images. A plate of 40-μm-thick GAGG single crystal ($Ce:Gd_3Al_2Ga_3O_{12}$) which has an excellent scintillation light yield and a short decay time of 53 ns[42] was used for the scintillator screen. The effective pixel size of the detector was measured to be 10 μm (9.9 μm at the position of the rotation axis). The FWHM of the line spread function (LSF) of the detector was determined to be 21 μm from its modulation transfer function (MTF) after the Coltman correction,[43] which was well fitted by a Lorentzian.

The image acquisition sequence for the proposed technique is shown in Fig. 2. A 3-step fringe scanning based on the equal sampling algorithm[38] was performed by continuously moving G2 and rotating the sample. The speed of G2 was tuned as it was moved by one pitch while the sample was rotated through 3 turns. From the three moiré images obtained for the same projection angle θ_{proj} for three different positions of G2, transmittance, differential-phase, and normalized-visibility images can be obtained. Tomographic reconstruction can be performed from the projection images obtained in the range of the projection angle $0 \leq \theta_{proj} < 180°$ because the white synchrotron X-ray beam is almost parallel. As such, 2.5 turns of the sample are required during image acquisition. Note that two sets of projection images can be obtained for tomographic reconstruction during 3 turns of the sample only by adding the projection images for another half turn of the sample, which can be used to reduce statistical errors. The field-of-view (FOV) can also be extended by performing so-called offset tomography using the 3-turn projection images.

For the demonstration of millisecond-order X-ray tomography using a fringe scanning method, a piece of wood was used as a sample. The sample was rotated with a speed of 33850 rpm, which corresponds to 4.43 ms for 2.5 turns of the sample. In the process, moiré images generated by the two gratings were acquired (see movie 1 in the online supplementary data at http://stacks.iop.org/APEX/11/122501/mmedia). The visibility of the moiré fringes was 31%, which was much higher than that obtained for the Fourier transform method reported in previous reports.[33,34] Note that this visibility is mainly determined by the spectrum of the white synchrotron X-ray beam with a wide bandwidth, i.e., the finite temporal coherence of the beam,[35] the fixed thickness of G1, which reduces the visibility of the self-image of G1 formed by the Talbot effect, and the finite thickness of G2 which cannot effectively block high-energy X-rays. The frame rate of the camera was set to be 127,500 fps and each moiré image was captured with a shutter speed of 7.8 μs. Figure 3 shows examples of transmittance, moiré-phase, and normalized-visibility images. The FOV of the images are 128 pixel × 64 pixel, which is limited by the maximum FOV of the CMOS camera at the given frame rate. For each image, 500 reference images were used. These were obtained from 1500 moiré images without the sample. A higher spatial resolution compared to that obtained using the Fourier transform method as reported in previous reports[33,34] is achieved using the fringe scanning method. The standard deviation of the transmittance and moiré-phase images in regions without the sample were 0.010 and 0.038 ($2\pi \times 0.0060$), respectively. Although the standard deviations are affected by the read-out noise of the camera depending on the frame rate, browning of the lenses in the X-ray image detector due to scattered X-rays, and the quality of the gratings in the FOV, the ratio of the standard deviation for the moiré-phase image compared to that of the transmittance image was much smaller than the values obtained for the Fourier transform method[33,34] because of the high visibility of the moiré fringes. Note that, as reported in a previous paper,[34] the effective energies of the transmittance and moiré-phase images are 24.2 and 27.1 keV, respectively for a weakly-absorbing sample. In addition, the moiré phase shift due to the sample is approximately proportional to $\partial\delta/\partial x$, where $1 - \delta$ is the real part of the refractive index of the sample for the effective-energy, when

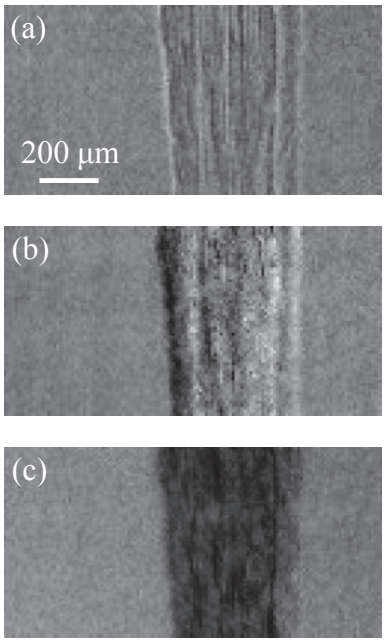

Fig. 3. (a) Transmittance, (b) moiré-phase, and (c) normalized-visibility images of a piece of wood [gray scales: (a) 0.83–1.16, (b) $-\pi/5$–$\pi/5$, (c) 0.27–1.73].

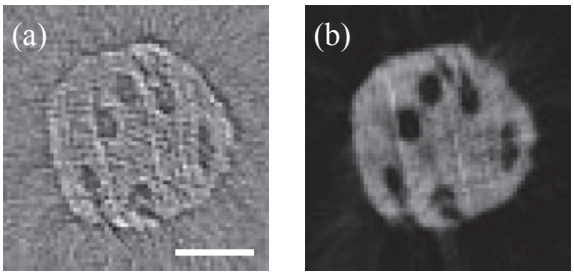

Fig. 4. Tomograms for β and δ, where $1-\delta$ and β are the real and the imaginary parts of the X-ray refractive index for effective energies [gray scales: (a) -3×10^{-9}–3×10^{-9}, (b) 0.0–4.0×10^{-7}, scale bar: 200 μm].

the absolute value of the moiré phase shift is within a range less than $\pi/2$.

Figure 4 shows examples of tomograms for β and δ, where β is the imaginary part of the refractive index of the sample for the effective energies [see movies 2 and 3 in the online supplementary data at http://stacks.iop.org/APEX/11/122501/mmedia for the tomograms of β and δ (68 pixel × 68 pixel, gray scale: -3×10^{-9}–3×10^{-9} and 0.0–4.0×10^{-7}, respectively)]. Each of the tomograms was reconstructed using a convolution-back projection algorithm from 113 projection images (339 moiré images captured in a net time of 2.66 ms). Note that although β is negligible and the enhanced edges in the transmittance images do not satisfy the mathematical conditions that are necessary for tomographic reconstruction, the contours of the internal structures in the sample are clearly seen in Fig. 4(a). The standard deviation of δ in regions without the sample was 9.4×10^{-9}, corresponding to a density resolution of 30 mg/cm^3 for water, which is approximately twice the value attained using the Fourier transform method as reported in a previous publication.[33] From the orthogonal views obtained from movie 3 in the online supplementary data at http://stacks.iop.org/APEX/11/122501/mmedia, it was confirmed that the spatial resolution in the axial direction was approximately 2 pixels, which is comparable to the spatial resolution of the X-ray image detector used.

In the experimentally obtained tomograms, no motion artifact was observed. This implies that displacement and distortion of the sample due to centrifugal forces was negligible during the measurement time. This assertion is reasonable when the centrifugal force on the sample is estimated. Given that the density of wood is less than 1 g/cm^3, the centrifugal force per axial length of the sample is less than 2×10^{-3} N/mm even when the sample is 1 mm apart from the rotation center, and thus the motion of the sample and the axis of the DC motor should be negligible with respect to the spatial resolution of a few tens of μm. Even if the sample is distorted by the centrifugal force, tomograms obtained under the influence of this force can still be reconstructed as long as the force balance is maintained and movement of the position of the rotation axis is negligible during the measurement time.

In summary, X-ray imaging based on X-ray grating interferometry was performed using a white synchrotron beam at BL28B2, SPring-8, Japan. By employing a fringe method, transmittance, moiré-phase, and normalized-visibility images with a spatial resolution of 21 μm were obtained for a piece of a wood with a frame rate of 127,500 and a shutter speed of 7.8 μs (Fig. 3). X-ray absorption and phase tomograms were also obtained for the sample with a measurement time of 4.43 ms (net time: 2.66 ms) (Fig. 4). The density resolution obtained using the fringe scanning method with high visibility moiré fringes was twice that achieved using the Fourier transform method. It should be noted that as previously described, another half turn of the sample (totaling 3 turns and corresponding to a time of 5.32 ms) can further improve the signal-to-noise ratio of the tomograms [see movies 4 and 5 in the online supplementary data at http://stacks.iop.org/APEX/11/122501/mmedia for the tomograms for β and δ (68 pixel × 68 pixel, grayscale: -3×10^{-9}–3×10^{-9} and 0.0–4.0×10^{-7}, respectively)].

The proposed approach can be applied to realize four-dimensional X-ray tomography[7,8,22,25,44,45] with spatial and temporal resolutions of a few tens of μm and a few ms, respectively, for the observation of unrepeatable phenomena in a sample that can be rotated at a high speed. Another application of the approach is high-throughput X-ray tomography, which can provide big data for deep learning. Higher temporal resolution and larger FOV should also be possible by exploiting advanced information processing techniques including compressed sensing[34,46,47] and interior tomography.[48,49] Such techniques not only make it possible to apply the proposed approach to large samples but also reduce radiation. Thus, the presented approach lays the foundation for a new frontier in 3D imaging by facilitating a level of imaging versatility that is not feasible using other techniques.

Acknowledgments The experiment was performed in SPring-8 (proposal numbers: 2015A1525, 2015B1263, 2016A1258, and 2016B1229). This research was supported by JSPS KAKENHI Grant Numbers JP15H03590, JP26600137, and JST CREST Grant Number JPMJCR1765.

1) R. Fitzgerald, Phys. Today **53** [7], 23 (2000).
2) A. Momose, Jpn. J. Appl. Phys. **44**, 6355 (2005).
3) K. A. Nugent, Adv. Phys. **59**, 1 (2010).

4) A. Snigirev, I. Snigireva, V. Kohn, S. Kuznetsov, and I. Schelokov, Rev. Sci. Instrum. **66**, 5486 (1995).
5) S. W. Wilkins, T. E. Gureyev, D. Gao, A. Pogany, and A. W. Stevenson, Nature **384**, 335 (1996).
6) P. Cloetens, R. Barrett, J. Baruchel, J.-P. Guigay, and M. Schlenker, J. Phys. D **29**, 133 (1996).
7) J. J. Socha, M. W. Westneat, J. F. Harrison, J. S. Waters, and W. K. Lee, BMC Biol. **5**, 6 (2007).
8) J. S. Lee, B. M. Weon, S. J. Park, J. H. Je, K. Fezzaa, and W. K. Lee, Nat. Commun. **2**, 367 (2011).
9) S. M. Walker, D. A. Schwyn, R. Mokso, M. Wicklein, T. Müller, M. Doube, M. Stampanoni, H. G. Krapp, and G. K. Taylor, PLoS Biol. **12**, e1001823 (2014).
10) A. Rack, M. Scheel, L. Hardy, C. Curfs, A. Bonnin, and H. Reichert, J. Synchrotron Radiat. **21**, 815 (2014).
11) M. P. Olbinado, X. Just, J.-L. Gelet, P. Lhuissier, M. Scheel, P. Vagovic, T. Sato, R. Graceffa, J. Schulz, A. Mancuso, J. Morse, and A. Rack, Opt. Express **25**, 13857 (2017).
12) M. P. Olbinado, J. Grenzer, P. Pradel, T. De Resseguier, P. Vagovic, M.-C. Zdora, V. A. Guzenko, C. David, and A. Rack, J. Instrum. **13**, C04004 (2018).
13) E. M. Escauriza, M. P. Olbinado, M. E. Rutherford, D. J. Chapman, J. C. Z. Jonsson, A. Rack, and D. E. Eakins, Appl. Opt. **57**, 5004 (2018).
14) C. David, B. Nöhammer, and H. H. Solak, Appl. Phys. Lett. **81**, 3287 (2002).
15) A. Momose, S. Kawamoto, I. Koyama, Y. Hamaishi, K. Takai, and Y. Suzuki, Jpn. J. Appl. Phys. **42**, L866 (2003).
16) T. Weitkamp, A. Diaz, C. David, F. Pfeiffer, M. Stampanoni, P. Cloetens, and E. Ziegler, Opt. Express **13**, 6296 (2005).
17) A. Momose, W. Yashiro, and Y. Takeda, Jpn. J. Appl. Phys. **45**, 5254 (2006).
18) F. Pfeiffer, T. Weitkamp, O. Bunk, and C. David, Nat. Phys. **2**, 258 (2006).
19) W. Yashiro, Y. Takeda, and A. Momose, J. Opt. Soc. Am. A **25**, 2025 (2008).
20) F. Pfeiffer, T. Weitkamp, O. Bunk, and C. David, Nat. Mater. **7**, 134 (2008).
21) W. Yashiro, Y. Takeda, A. Takeuchi, Y. Suzuki, and A. Momose, Phys. Rev. Lett. **103**, 180801 (2009).
22) A. Momose, W. Yashiro, H. Maikusa, and Y. Takeda, Opt. Express **17**, 12540 (2009).
23) T. H. Jensen, M. Bech, O. Bunk, T. Donath, C. David, R. Feidenhans'l, and F. Pfeiffer, Phys. Med. Biol. **55**, 3317 (2010).
24) W. Yashiro, Y. Terui, K. Kawabata, and A. Momose, Opt. Express **18**, 16890 (2010).
25) A. Momose, W. Yashiro, S. Harasse, and H. Kuwabara, Opt. Express **19**, 8423 (2011).
26) H. Kuwabara, W. Yashiro, S. Harasse, H. Mizutani, and A. Momose, Appl. Phys. Express **4**, 062502 (2011).
27) A. Momose, H. Kuwabara, and W. Yashiro, Appl. Phys. Express **4**, 066603 (2011).
28) W. Yashiro, S. Harasse, K. Kawabata, H. Kuwabara, T. Yamazaki, and A. Momose, Phys. Rev. B **84**, 094106 (2011).
29) S. Kibayashi, S. Harasse, W. Yashiro, and A. Momose, AIP Conf. Proc. **1466**, 261 (2012).
30) M. P. Olbinado, P. Vagovič, W. Yashiro, and A. Momose, Appl. Phys. Express **6**, 096601 (2013).
31) W. Yashiro and A. Momose, Opt. Express **23**, 9233 (2015).
32) W. Yashiro, P. Vagovič, and A. Momose, Opt. Express **23**, 23462 (2015).
33) W. Yashiro, D. Noda, and K. Kajiwara, Appl. Phys. Express **10**, 052501 (2017).
34) W. Yashiro, R. Ueda, K. Kajiwara, D. Noda, and H. Kudo, Jpn. J. Appl. Phys. **56**, 112503 (2017).
35) W. Yashiro, D. Noda, and K. Kajiwara, Opt. Express **26**, 1012 (2018).
36) V. Revol, C. Kottler, R. Kaufmann, U. Straumann, and C. Urban, Rev. Sci. Instrum. **81**, 073709 (2010).
37) M. Takeda, H. Ina, and S. Kobayashi, J. Opt. Soc. Am. **72**, 156 (1982).
38) J. H. Bruning, D. R. Herriott, J. E. Gallagher, D. P. Rosenfeld, A. D. White, and D. J. Brangaccio, Appl. Opt. **13**, 2693 (1974).
39) H. Schreiber and J. H. Bruning, in *Optical Shop Testing*, ed. D. Malacara (Wiley, Hoboken, NJ, 2007) 3rd ed., Chap. 14.
40) E. Hack and J. Burke, Rev. Sci. Instrum. **82**, 061101 (2011).
41) Web [http://www.spring8.or.jp/en/about_us/whats_sp8/facilities/accelerators/storage_ring/].
42) K. Kamada, T. Endo, K. Tsutumi, T. Yanagida, Y. Fujimoto, A. Fukabori, A. Yoshikawa, J. Pejchal, and M. Nikl, Cryst. Growth Des. **11**, 4484 (2011).
43) J. W. Coltman, J. Opt. Soc. Am. **44**, 468 (1954).
44) L. Xu, R. C. Chen, G. H. Du, Y. M. Yang, F. X. Wang, B. A. Deng, H. L. Xie, and T. Q. Xiao, Sci. Rep. **6**, 32380 (2016).
45) A. Ruhlandt, M. Töpperwien, M. Krenkel, R. Mokso, and T. Salditt, Sci. Rep. **7**, 6487 (2017).
46) M. H. Li, H. Q. Yang, and H. Kudo, Phys. Med. Biol. **47**, 2599 (2002).
47) D. L. Donoho, IEEE Trans. Inf. Theory **52**, 1289 (2006).
48) Y. Ye, H. Yu, Y. Wei, and G. Wang, Int. J. Biomed. Imaging **2007**, 63634 (2007).
49) H. Kudo, M. Courdurier, F. Noo, and M. Defrise, Phys. Med. Biol. **53**, 2207 (2008).